

# Laser Ion Acceleration from Mass-Limited Targets with Preplasma

K. V. Lezhnin,<sup>1,2</sup> F. F. Kamenets,<sup>2</sup> T. Zh. Esirkepov,<sup>3</sup> S. V. Bulanov,<sup>3,4</sup> O. Klimo,<sup>1,5</sup> S. Weber,<sup>1</sup> and G. Korn<sup>1</sup>

<sup>1</sup>*Institute of Physics of the ASCR, ELI-Beamlines, Na Slovance 2, 18221 Prague, Czech Republic*

<sup>2</sup>*Moscow Institute of Physics and Technology, Institutskiy per. 9, Dolgoprudny, Moscow Region 141700, Russia*

<sup>3</sup>*Kansai Photon Science Institute, 8-1-7 Umemidai, Kizugawa, Kyoto 619-0215, Japan*

<sup>4</sup>*A. M. Prokhorov General Phys. Inst. of RAS, Vavilov Str. 38, Moscow 119991, Russia*

<sup>5</sup>*Faculty of Nuclear Sciences and Physical Engineering,  
Czech Technical University in Prague, 11519 Prague, Czech Republic*

(Dated: May 29, 2022)

The interaction of high intensity laser radiation with mass-limited target exhibits significant enhancement of the ion acceleration when the target is surrounded by an underdense plasma corona, as seen in numerical simulations. The self-generated quasistatic magnetic field squeezes the corona causing the intensification of a subsequent Coulomb explosion of the target. The electric field intensification at the target edges and plasma resonance effects result in the generation of characteristic density holes and further contributes to the ion acceleration.

Keywords: Relativistic laser plasmas, Ion acceleration, Quasi-static magnetic field, Particle-in-Cell simulation

PACS numbers: 52.38.Kd, 52.65.Rr

## I. INTRODUCTION

High energy ion generation in the interaction of intense laser pulses with mass-limited targets is promising for applications in a wide range, from the development of ion sources for medicine and the fast ignition of controlled thermonuclear fusion to the investigation of warm dense matter, high energy density phenomena, and laboratory astrophysics (see review articles [1–5] and references therein). Mass-limited targets otherwise called reduced mass targets have a finite transverse size comparable with the laser focal spot diameter [6–9]. Their principal advantage is that an intense laser pulse can remove much more electrons from it than from a wide and thick target. This generates a greater electrostatic potential thus enhancing the ion acceleration. In wider targets, electrons from the periphery additionally reduce the ion acceleration quickly smoothing out the electric potential, while in thick targets, the laser radiation cannot reach deeper layers.

The advantage of mass-limited targets is best seen with isolated clusters, from which an intense laser sweeps all the electrons. Then the Coulomb explosion occurs: the ions are accelerated under the repulsion force of uncompensated electric charge. A pure Coulomb explosion provides an isotropic ion acceleration with very characteristic energy spectrum, where a large number of ions acquire a high energy [10].

When the laser radiation can not penetrate inside the target deeper than the skin depth, it heats electrons creating a plasma sheath with a strong electric charge separation. The latter causes the ion acceleration in the target normal sheath acceleration (TNSA) regime [11–13]. In mass-limited targets, this regime can give a substantial contribution to the ion acceleration when the laser pulse power is far from being enough to wipe all the electrons.

For sufficiently high intense laser pulses and optimally dense targets, the laser radiation pressure pushes the target as a whole in the propagation direction, while the target remains, on average, mostly quasi-neutral. This is the regime of the radiation pressure dominated acceleration (RPDA) of ions [14–17]. A tailored laser pulse can provide in principle unlimited ion acceleration [18]. In the case of a mass-limited target, the RPDA of ions can be stable even if the target is initially off-axis [19]. A combination of the RPDA and a subsequent Coulomb explosion of a thick target leads to a directed Coulomb explosion regime of the ion acceleration [20].

In general, a laser system produces a high-intensity short-duration (main) pulse on top of a relatively low-intensity nanosecond (background) amplified spontaneous emission (ASE), possibly with a few prepulses. The main-pulse-to-background intensity ratio is called the laser pulse contrast. When a laser pulse with a finite contrast irradiates a solid target, preplasma is created before the main pulse arrival. Preplasma is a plasma region where the density gradually drops from values typical to solid state at some depth in the target down to a value well below the critical density. Preplasma created around structured snow-targets irradiated by intense laser pulses facilitates the efficient ion acceleration via the edge field intensification effect [7, 8]. The main pulse interacting first with preplasma exhibits regimes typical to gaseous targets, especially when the plasma density is near-critical. Under these conditions, laser radiation can form a long-living quasi-static magnetic dipole leading to the Magnetic Vortex Acceleration regime [21, 22], or can create a shock wave putting into effect the Shock Wave Acceleration [23]. While the main pulse loses its energy in preplasma it can also self-focus due to relativistic effects [24], thus an optimised preplasma can crucially enhance the ion acceleration [25].

Here we investigate how the above mentioned ion acceleration mechanisms reveals itself depending on the geometry of a mass-limited target and a plasma corona around it. We carry out two-dimensional (2D) Particle-in-Cell (PIC) simulations using the REMP code based on the density decomposition scheme [26]. We describe the effects occurring in the presence of a plasma corona around a mass-limited target: the enhancement of the Coulomb explosion of the ion core of the target due to the density squeezing by the quasistatic magnetic field, formation of a density hole near the tip of the target due to plasma resonance, etc. The paper is organized as follows. In the next Section, we describe the laser and target parameters and the simulation configuration. In Section III, the results of PIC simulations of the laser pulse interaction with mass-limited targets in a wide range of the irradiation parameters are presented. There we discuss the effects of magnetic squeezing and electric field intensification at the target edge on the ion acceleration. In Section IV, we consider the high power limit when the ion acceleration occurs in the radiation pressure dominated acceleration regime. In the concluding Section, we summarize the results obtained.

## II. SIMULATION CONFIGURATION

In order to investigate the processes that occur during the interaction of a relativistically strong laser pulse with a mass-limited water ice target surrounded by a plasma corona, we conduct a series of 2D PIC simulations. The laser pulse is obliquely incident on the target as is shown in the upper panel of Fig. 1.

The plasma corona with a typical size of the order of several tens of micrometers plays an important role in the laser interaction with mass-limited targets [6]. When it is created due to a finite contrast of the laser pulse, it has a typical density profile consisting of three regions (see also Ref. [25]). The first region is a plateau with the solid density, corresponding to unperturbed portion of the target. The second region has the density profile which can be approximated by the Gaussian function as shown in the lower panel of Fig. 1. There the density decreases from the solid density value to the critical density,  $n_{cr} = \pi/r_e\lambda^2$ , corresponding to the laser wavelength  $\lambda$ . Here  $r_e = e^2/m_e c^2 \approx 2.8 \times 10^{-13}$  cm is classical electron radius. In the third region, the plasma density linearly drops with a substantially larger scale.

In our simulations, the target has the shape of an ellipsoid, so that the same density value curves are ellipses. For such a shape it is enough to describe the density profile along the major semi-axes. We assume the following density profile. The density decreases from maximum according to the Gaussian function down to  $n_{cr}$ , then it linearly drops down to  $0.1n_{cr}$ , then it is truncated to zero. In order to restrict the total number of quasi-particles representing plasma (which amounts to  $1.2 \times 10^6$ ), we limit the plasma density by the cutoff at

$10n_{cr}$ . For moderate laser intensities, when the laser radiation pressure is not dominant in the interaction, this artificial cutoff does not significantly affect the simulation results, as justified by a number of test simulations performed without a density cutoff (note the analogous computational trick used in Ref. [6]).

Here we present the results for a relatively high eccentricity,  $\epsilon = 0.995$ , of the ellipsoid representing the target shape. This choice allows emphasizing the effects of a quasistatic magnetic field generated during the interaction. In preliminary simulations (not shown here) we have found that for targets with a smaller eccentricity the quasi-static magnetic field is not sufficiently symmetrical with respect to the target major axis. The ion energy reaches maximum when the magnetic field is generated in a symmetrical way (this is applicable for moderate laser intensities, when the laser radiation pressure does not dominate the interaction). If the target has the form of a foil (in terms of ellipsoid target, it means that the major semiaxis is substantially larger than the laser focal spot size), the electrons move away from the region of irradiation, along the target surface, so that the associated quasi-static magnetic field disperses along the target surface and eventually dissipates.

The laser pulse has a super-Gaussian profile with an index of 4, so that the laser pulse intensity time profile is described by the function  $I = 1.37 \times 10^{18} \times a_0^2 (2)^{-(2t/\tau)^4} \times (1\mu\text{m}/\lambda)^2 \text{W}/\text{cm}^2$ . The transverse laser pulse profile is also super-Gaussian with an index of 4. The dimensionless amplitude,  $a_0 = eE_0/m_e\omega c$ , characterizes the laser electric field strength,  $E_0$ . Here  $\omega = 2\pi c/\lambda$ . The laser pulse duration is  $\tau = 15\lambda/c$ , its focal spot diameter is  $5\lambda$ . The laser pulse is p-polarized, i.e., its electric field vector is in the simulation plane  $(x, y)$ . In our simulations, the laser amplitude varies from  $a_0 = 3$  to  $a_0 = 134$ , which corresponds to the peak laser power in the range from 5 TW to 10 PW. The laser focal plane is at the sharp edge of the target where the density is  $n_e = n_{cr}$ , if not stated otherwise. The laser pulse is obliquely incident on the target at the angle of 45 degrees. This configuration is chosen to maximize the laser energy transmission to the target. For references concerning the dimensional values of the target density, laser energy and intensity, etc, the laser wavelength can be assumed to be  $\lambda = 0.8\mu\text{m}$ . For the scaling into the high laser power, we used the same profile but multiplied by some factor in accordance with the  $a_0 = \pi n_e l_0 / n_{cr} \lambda$  criteria, where  $l_0$  is the target thickness (the size along the minor axis).

Our target is composed of electrons, protons, and oxygen ions corresponding to frozen water,  $\text{H}_2\text{O}$ . The following mass ratios has been used:  $m_p/m_e = 1836$ ,  $m_O/m_p = 16$ . As is well known, one of the parameters that could influence the ion acceleration significantly is the ionization degree,  $Z$ , and its spatial distribution [27]. For the sake of simplicity, in our simulations we assume a homogeneous spatial distribution of the ionization degree, which is fixed during the simulation's run and does not exceed the maximum value of  $Z_{\text{max}}$ . We estimate

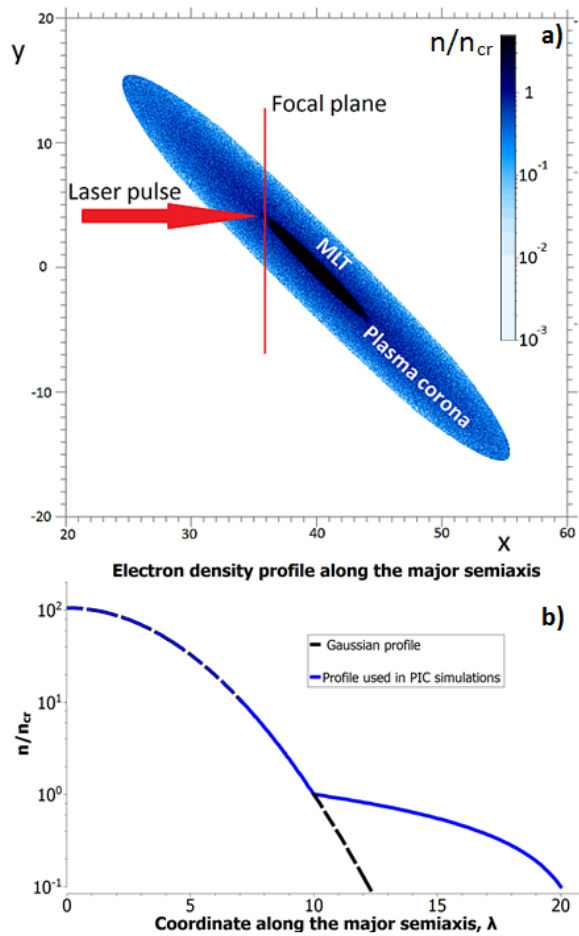


FIG. 1. a) A configuration of the laser interaction with the mass-limited target (MLT), the electron density, the laser propagation direction and the focal plane. Hereafter, all spatial dimensions are normalized to laser wavelength  $\lambda$ , temporal one - to laser period  $2\pi/\omega_0$ , densities are normalized to critical density  $n_{cr}$ , and electromagnetic fields are normalized to  $E_0 = m_e\omega_0 c/e$ . b) The electron density profile along the major semiaxis. Hereafter we call the Gaussian profile as “shortened” and complex one marked with blue as “extended”.

this ionization degree maximum within the framework of the optical field ionization model. Following Ref. [27], we obtain  $Z_{max}^{2-4} \approx C_a \times a_0$ , with  $C_a \sim 12$ . Depending on the laser amplitude, in our simulations we initially set oxygen ions with the ionization degree of +3, +5, +7 and +8.

In our simulations, the grid mesh size is  $\lambda/32$  in each spatial direction. For moderate laser intensities, the simulation box has the size of  $80\lambda \times 120\lambda$ . For higher laser intensity,  $a_0 > 20$ , the simulation box is larger,  $200\lambda \times 200\lambda$ , in order to avoid stronger unphysical effects from the boundaries. The boundaries are absorbing for particles. For the electromagnetic radiation, the boundaries are periodical. The space and time values are given in units of the laser wavelength and period, i.e.,  $\lambda$  and  $2\pi/\omega$ , respectively.

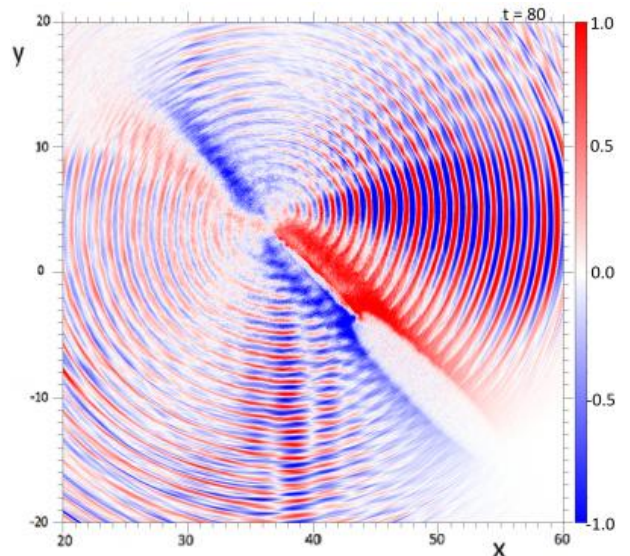


FIG. 2. Magnetic field distribution in the  $(x, y)$  plane at  $t = 80$  for  $a_0 = 3$  case showing the laser pulse scattering at the target tip and reflection by the overdense plasma region.

### III. SIMULATION RESULTS

We start our consideration with the case of a 5 TW laser pulse, corresponding to  $a_0 = 3$ . While such the laser power can be considered relatively low in comparison with the up-to-date laser systems, it allows us to clarify a number of effects that can occur in the high-power limit.

Fig. 2 shows the magnetic field distribution at a final stage of the laser pulse interaction with the target. About 60% of the laser pulse energy passes through, because of the location of the focus at the target tip, where plasma is underdense. Nevertheless, a substantial part of the laser energy is absorbed: eventually about 35% is transferred to the particle energy. One of the absorption mechanisms is the plasma resonant absorption, because for a p-polarized electromagnetic wave obliquely incident on the target the projection of the vector of electric field on the plasma density gradient does not vanishes,  $\vec{E} \cdot \nabla n \neq 0$  (for details of the plasma resonance phenomenon see, e.g., Refs. [28, 29]). A small part of the laser pulse is scattered at the target tip and specularly reflected by the overdense plasma region, as is clearly seen in Fig. 2. Scattered radiation has a form a cylindrical electromagnetic wave with an inhomogeneous distribution of the field amplitude. The transverse modulations seen in the transmitted and reflected pulses are due to strong plasma density modulations created by the incident laser pulse.

During the laser pulse interaction with the plasma corona, it undergoes relativistic self-focusing, which can be seen in a slight increase of the transmitted pulse amplitude. We also note that the electric field strength at the target tip increases due to the edge intensification of electromagnetic field and the rise of plasma resonance

[30].

A well-pronounced temporal periodicity of the maximum amplitude field (with the frequency close to that of the laser) and the absence of substantial field enhancement in the case of s-polarized pulse indicate the effect of the plasma resonance at the tip of the overdense target.

Considering the simulation results for different initial laser amplitude  $a_0$ , we find the following properties of the instantaneous electric and magnetic field strength maximum,  $E_i$  and  $B_i$ , respectively. For  $a_0 < 10$ ,  $B_i \approx 2a_0$ , which is merely due to a transient standing wave formed during the laser pulse reflection from the target and due to just logarithmic enhancement of the magnetic field in the resonance region (see Ref. [31]). Weaker reflection is observed for  $a_0 \geq 10$ , correspondingly, in this range  $B_i \leq 1.5a_0$ . The dependence of the instantaneous electric field strength maximum on the laser amplitude changes from  $E_i \approx 6a_0$  at  $a_0 = 1$  to  $E_i \approx 2a_0$  at  $a_0 \geq 10$ .

### A. Magnetic Squeezing

Fig. 3 shows the evolution of the electron density distribution at the bottom part of the target, quite far from the laser pulse focus location, for the case of  $a_0 = 3$ . At  $t = 80 \times 2\pi/\omega$ , the density modulations with the wavelength equal to that of the laser are seen along the target. At later time, the plasma corona is squeezed. Eventually a high-density filament is formed, as seen at  $t = 140 \times 2\pi/\omega$ . The squeezing takes place for every kind of particles on their own timescale determined by their charge-to-mass ratio.

We also observe the appearance of the proton depletion regions in the upper part of the corona (see Fig. 4), where the quasistatic magnetic field is maintained for a long time, making a substantial impact on the ion acceleration as well (hole 2, see Fig. 4 and 6).

Effect of the corona squeezing is strongly correlated with the magnetic field evolution. Figures 5 and 6 show the magnetic field evolution at the same instants of time. Laser pulse interacts with the electrons from the corona, forcing them to circulate around the upper and lower parts of the target in the  $(x, y)$  plane. The electric current carried by the electrons generates the magnetic field, i.e., the magnetic vortex structure is being created. It is noticeable that the maximum value of the generated quasistatic magnetic field exceeds the maximum laser pulse amplitude by a factor of more than two. As is well known, the magnetic vortex formation is a common process in the laser irradiated underdense plasma [32] having a density gradient [21]. The crucial parameter for the vortices is the density gradient as it determines their lifetime and propagation velocity. We have considered various configurations of the corona density distribution, and it turns out that density profile should be gentle enough ( $\approx 0.1n_{cr}/\mu\text{m}$ , in agreement with [21]) in order to keep the vortices in the corona for relatively long time. However the plasma density gradient should not be too small

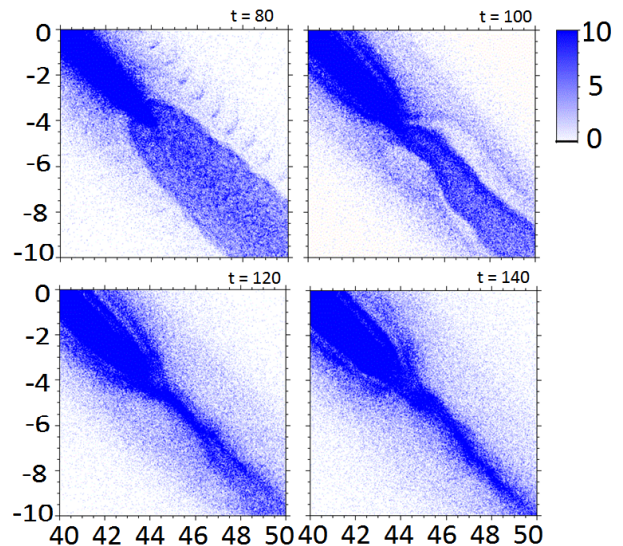


FIG. 3.  $a_0 = 3$ . Electron density distribution at  $t = 80, 100, 120$  and  $140$ . The underdense corona squeezing can be seen. Apart from that, the overdense part of the target is being shaped by the magnetic field.

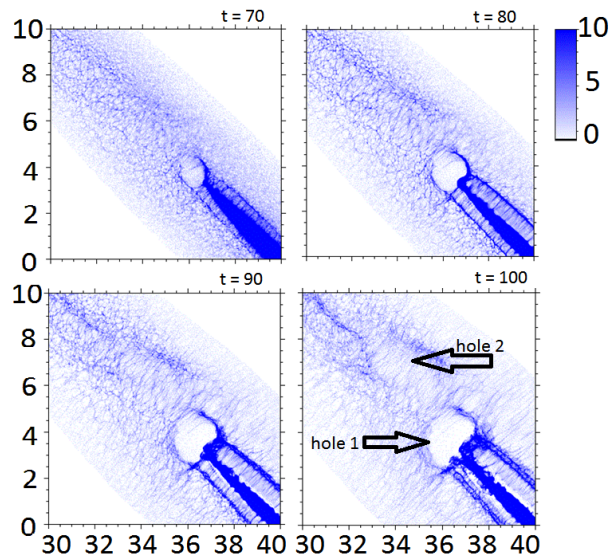


FIG. 4.  $a_0 = 3$ . Proton density distribution at  $t = 70, 80, 90$  and  $100$ . The hole appearance in the upper corona regions can be seen. The overdense part of the target is being compressed by the magnetic field.

because the vortices do not move in this case. Moreover, the geometry of the underdense region affects the vortex formation dramatically. This is due to the strong connection with the number of electrons trapped by the magnetic field of the pulse—the more electrons laser pulse sees during the propagation in the corona, the more stable magnetic field is generated. Propagating along the major semiaxis of the ellipsoid, these vortices force corona



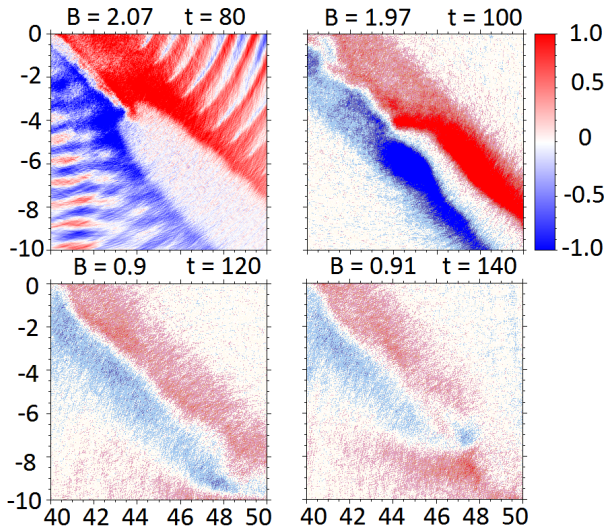


FIG. 5.  $a_0 = 3$ . Distribution of the  $z$ -component of the magnetic field in the lower target region at  $t = 80, 100, 120$  and  $140$ . The appearance of the quasistatic magnetic field corresponds to the hole in proton density, which can be explained by the vortices propagating along the major semi-axis, compressing the target and then slowly decreasing due to the electron expansion to vacuum.

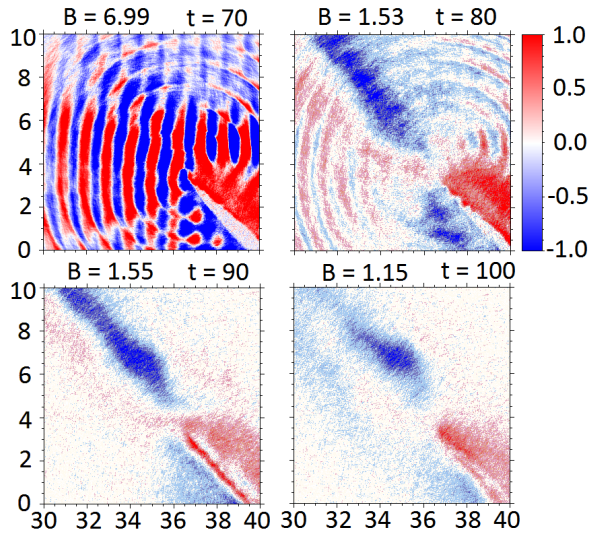


FIG. 6.  $a_0 = 3$ . Distribution of the  $z$ -component of the magnetic field in the upper target region at  $t = 70, 80, 90$  and  $100$ . Vortices propagate along the major semi-axis, compress the target and then slowly decrease due to the electron expansion to vacuum.

compression due to the magnetic pressure and then their amplitude gently decreases due to the expansion of the electrons to vacuum (Fig. 6).

Proton component of the target experiences the squeezing on its own timescale. From initial ellipsoidal layer with the density below the critical one, it is being increased at least by a factor of 5, which leads to the

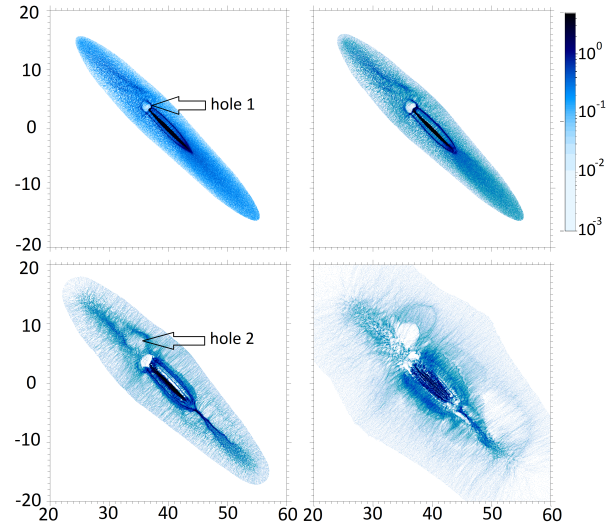


FIG. 7.  $a_0 = 3$ . Distribution of the proton density at  $t = 80, 100, 120$  and  $200$ . The hole boring in the upper corona regions and the corona squeezing in the bottom corona part can be seen.

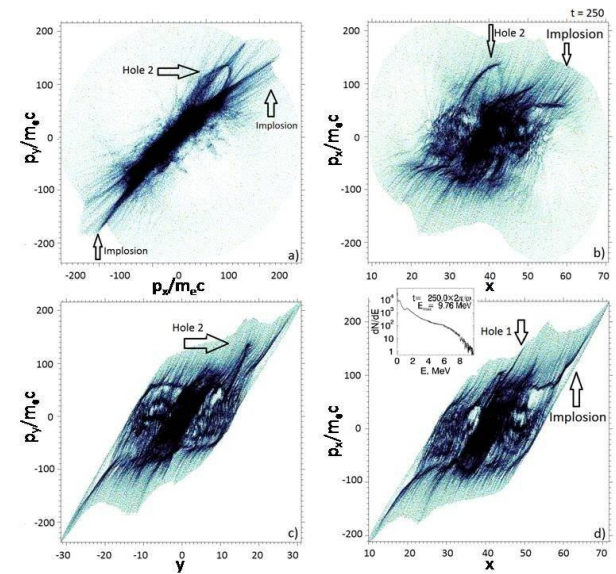


FIG. 8.  $a_0 = 3$ . Proton phase space and the energy spectrum ( $(p_x, p_y)$ ,  $(x, p_y)$ ,  $(y, p_y)$ , and  $(x, p_x)$  for  $t = 250$  (a), (b), (c), and (d), respectively); protons accelerated from both holes can be seen along with the magnetic squeezing effect. Inset: proton energy spectrum,  $E_{\max} \approx 10$  MeV.

more energetic Coulomb explosion than in more dense but also more quasi-neutral central part of the target.

We observe such effect in our simulations—we detect that for the case of  $a_0 = 3$  we get at least by an order of magnitude larger positive-signed total charge density than we could possibly had by removing all the electrons from the target without any pre-compression (see Fig. 9). All the "hair" with the largest energies in the configuration on the  $(p_x, p_y)$  distribution in Fig. 8 correspond

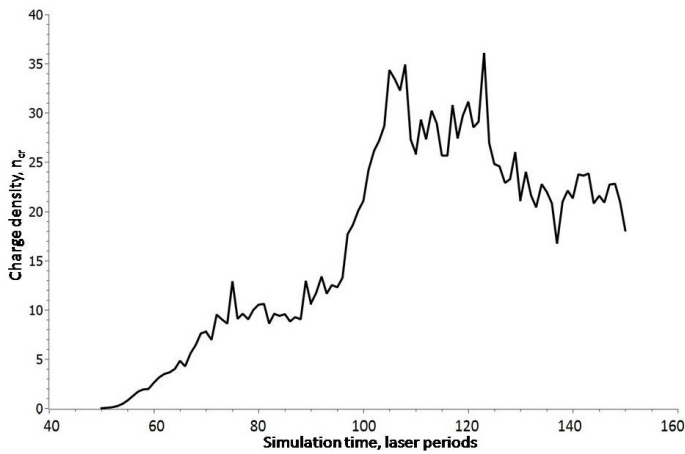


FIG. 9.  $a_0 = 3$ . Maximum charge density distribution in bottom corona region ( $44 < x < 50$ ,  $-10 < y < -4$ , see Fig. 3). We see a substantial increase of charge density at  $t = 120$ , when the Coulomb explosion of this region initiates (see Fig. fig5)

to this type of acceleration.

Similar effect also takes place in the upper corona region (hole 2). Pre-accelerated by the magnetic field, it eventually experiences the Coulomb explosion. Finally, it gives one of the most energetic populations of accelerated protons in the system, see  $(x, p_y)$  and  $(y, p_y)$  phase planes in Fig. 8.

It is also notable that the magnetic field penetrates into the overdense target region (see Figs. 5 and 6). As the solid state target part is always rich with electrons, the magnetic field would be sustained here for much longer time in comparison with corona vortices. These fields affect the ion acceleration process, boring the gaps and pushing the external target layers along the minor semi-axis, directing the acceleration of the protons (see Fig. 7).

Although there is an isotropic component of the proton momentum distribution (see Fig. 8,  $(p_x, p_y)$  plot) that can originate from the Coulomb explosion of an external layer of the underdense corona, the most energetic particles (and also the largest fraction of protons) are distributed in the vicinity of the diagonal  $p_y = p_x$  on a corresponding phase distribution plot (see Fig. 8). This strong anisotropy is in a tight connection with the geometry of the target having the form of a high eccentricity ellipsoid. The target can be regarded locally as a charged plane with the electric field orthogonal to the major semi-axis. However, there are some deviations from the main direction—filaments in the distribution of protons in the phase plane. Some of the proton beams contain substantial number of particles compared with the isotropic component. For example, two filaments seen in the  $(x, p_y)$  plot (the curved one around  $x \approx 35 - 40$  and the plane one around  $\approx 52 - 60$ ); even though they do not correspond to the maximum energy value, they are at least an order of magnitude more energetic than the

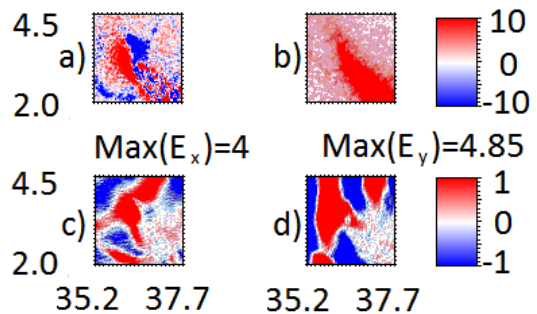


FIG. 10. a) charge density distribution around the target's tip; b) proton density distribution around the target's tip; c) and d):  $E_x$  and  $E_y$  electric field components. All graphs are presented at  $t=60$ , simulation for  $a_0 = 3$  laser pulse. Strong charge separation, corresponding field enhancement and starting point of proton acceleration are seen.

particles in the central part of the target. Taking into account that the initial central density is 10 times larger than the maximum corona density, we can conclude that the magnetic squeezing does have a positive effect, providing larger initial density for the Coulomb explosion of the corona.

## B. Edge field intensification and plasma resonance

We note that we do not see substantially large magnetic fields in the vicinity of the target tip (hole 1). Fig. 7 shows how the proton density evolves for 80, 100, 120 and 200 laser periods. As the laser pulse is focused on the sharp edge of the target, the electric field is amplified significantly in this region, which in its turn bores a hole in the proton density. The strong charge separation is observed at the sharp edge of the target for the whole period of laser propagation through the target, see Fig. 10. This hole might be associated with the plasma resonance [33] and edge field amplification [30, 31, 34] which can lead to the particle acceleration from the target's edge and hole 1 formation (see Figs. 10 and 11).

Plasma resonance is attributed to the enhancement of the electric field in the region of critical plasma density. The maximum electric field amplitude in nonlinear Langmuir oscillations excited at the resonance surface is determined by the wave breaking process (see Ref. [29] and literature cited therein). This results in the fast electron component generation and in the light ion acceleration. The light ion emission from the resonant region has been observed in our simulation. The light ion acceleration occurs under action of the pondermotive force that arises in the high-frequency field localized in the plasma resonance region [29, 33]. These ions are accelerated to the energies of the order of  $\mathcal{E}_i \approx Z\mathcal{E}_E$ , where  $\mathcal{E}_E \approx m_e v_E^2 / 2 = e^2 E_m^2 / 2m_e \omega^2$ ,  $E_m$  is the electric field in the plasma resonance region, corresponds to the electron quiver energy, and  $v_E$  is the electron quiver velocity.

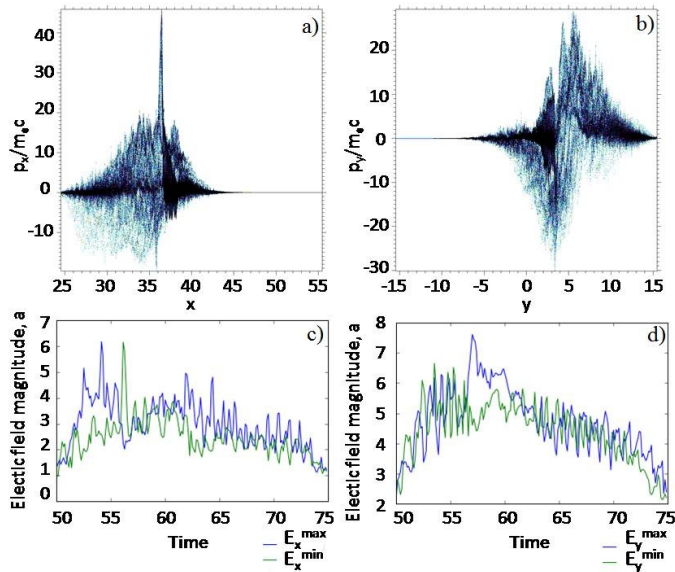


FIG. 11.  $a_0 = 3$ . a) and b): proton phase distributions in the planes  $(x, p_x)$  and  $(y, p_y)$  for  $t = 60$ ; the peak of proton momentum magnitude at  $(x = 37, y = 4)$  corresponds to plasma resonance at the sharp edge of the target. c) and d): distribution of electric field  $E_x$  and  $E_y$  projections amplitude; MAX and MIN denote to maximum positive and negative projections of the electric field in the resonant region (hole 1, see Figs. 4 and 7)

The proton energy, in our case, is approximately equal to  $a_0^2 m_e c^2 / 4$  which is of the order of 0.5 MeV for protons in case of  $a_0 = 1$ , corresponding to the electron quiver velocity. The ion phase distributions and charge density, proton density and projections of the electric field around the target tip can be seen in Fig. 10.

All these processes lead to the energy spectrum that is shown in Figure 12. We present two spectra—one for the target discussed above and another with the flat density profile in order to demonstrate how the density gradient impacts the maximum ion energy. Targets have the same shape of ellipsoid and the flat target is limited by the ellipsoid with semiaxes of  $1\mu\text{m} \times 10\mu\text{m}$ . As we see, implementing targets with density gradients leads to the proton energy increase up to 5 MeV. The maximum value of proton energy for corona-equipped target equals to  $\approx 16\text{MeV}$ , which can be considered as advanced acceleration level with the considered type of terawatt laser. The use of the corona-equipped target also provides better energy transmission, which is about 32% against 19% for the case of the flat target.

### C. High power limit

Here we discuss the physical processes that dominate the laser-target interaction in the limit of higher peak laser power. We show the results of the PIC simulations with the same target but with the larger laser amplitude

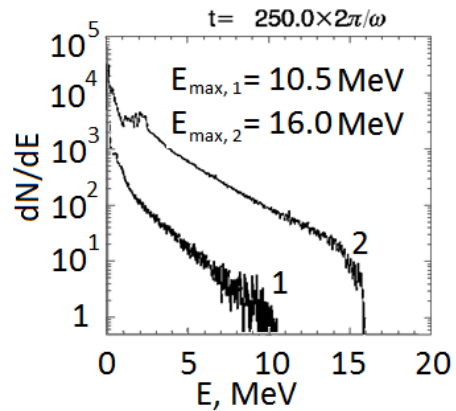


FIG. 12. Energy spectrum for flat-profile target (1) and inhomogeneous-profile target ("extended" corona, see Figure 1) setup (2),  $a_0 = 3$ .

$a_0$ . We take it equal to 20, which corresponds to 200 TW laser power. In this high field amplitude limit, the light ion acceleration is less pronounced because of the non-linear saturation of the resonance due to aperiodicity of plasma oscillations caused by the relativistic effects.

Besides, the fraction of the radiation that passes through the target has the amplitude increased to about  $\approx 20\%$ , which might be attributed to the self-focusing in the plasma corona, see Fig. 13.

The configuration of the target provides a high-level pulse energy transfer to the plasma and fast particle energy, energy transfer is about 52%. We note that the energy transfer in the flat-density profile targets is lower, about 35%. During the interaction with the laser pulse, the electrons are being heated and expand into the vacuum, generating a strong charge separation along with the heavy oxygen ions with uncompensated charge that contribute to the repelling field, in which the protons are being accelerated. Ions are seen to move in two shell way (see Fig. 14, c and d). The first shell of protons moves with higher speed and only afterwards, the shell of oxygen ions moves with lower velocity as seen in Fig. 14. Corresponding electric field could be seen at  $E_x$  (the symmetrical picture can be seen for  $E_y$  as well) distribution figure as well - inner repelling fields are for oxygen shell and outer - for protons. In case of extended corona we observe the maximum energies of 160 MeV protons and 14 MeV/u oxygen ions with the angle and energy distributions presented in Figure 15. With the exponential corona, we derived maximum energies at least 10% larger. Similar results have been obtained in Ref. [8].

As it has been shown in Ref. [19], the finite pointing precision of the laser imposes constraints on the maximum attainable energies of accelerated ions. However, while it is still true for the considered type of the target, the shift of the focus can give rise to a number of the effects that also provide energetic particles, even though their maximum energy is a factor of 1.5 smaller. For moderate laser power, we still observe that the most en-



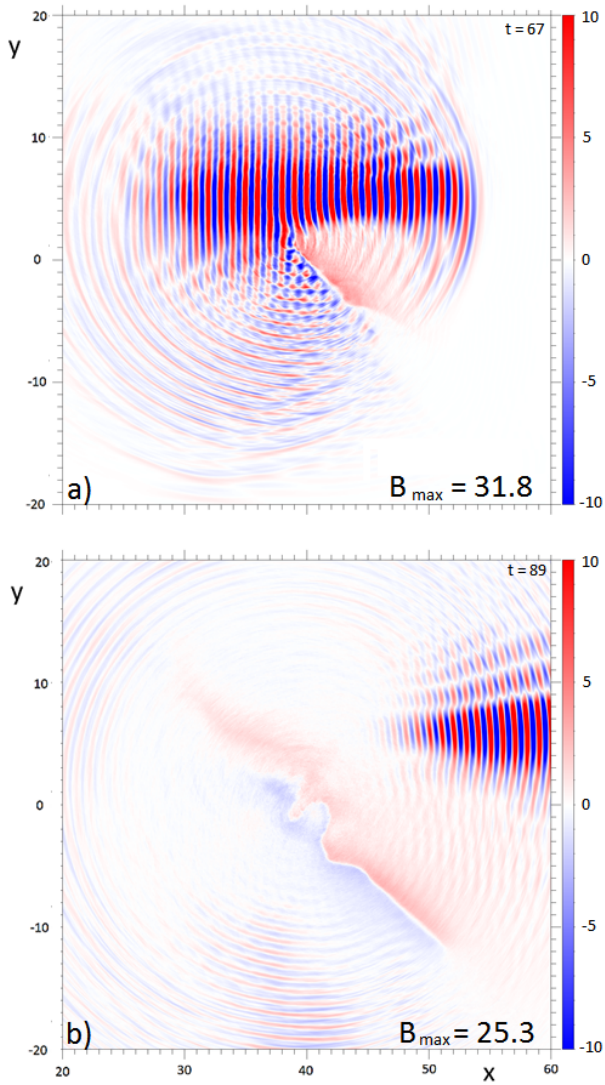


FIG. 13. Self-focusing for  $a_0 = 20$  laser pulse in the plasma corona. a) The  $z$ -component of the magnetic field in the  $(x, y)$ -plane at  $t = 67$ . b) The same as in the frame a) at  $t = 89$ .

ergetic particles form two opposite directing streams that are emitted from the target's tip. This is a consequence of both plasma resonance and edge field intensification, which give larger maximum field amplitudes.

In the limit of the ultrahigh laser powers ( $\approx 10$  PW) we can observe that these targets along with oblique incidence do not allow to reach the highest energies. Using the scaling parameter  $a_0 = \varepsilon = 2\pi n_e e^2 l / m_e \omega c$  (see Refs. [35, 36]), we derive that the maximum energy of the ions is below 1 GeV, while for normal incidence and thicker central part of the target we can get energies larger at least by a factor of two. Here two mechanisms come into play. The first of them is the RPDA, when the laser pulse pressure wipes out the central—the densest part of the target and after that, it undergoes a Coulomb explosion according to Ref. [20], reaching the maximum energy of

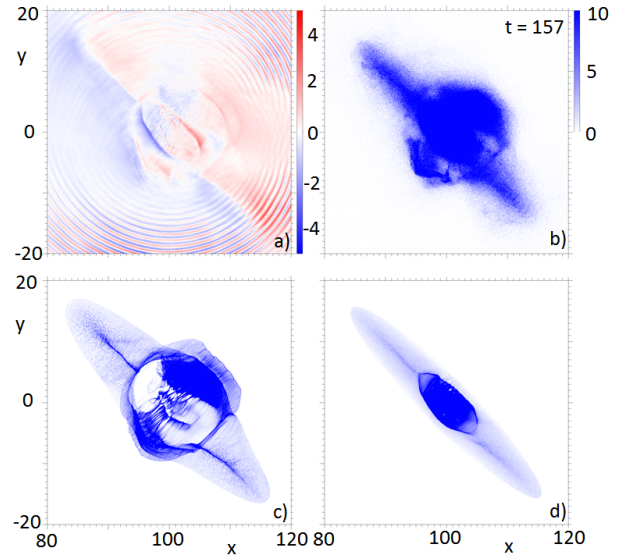


FIG. 14. a) The  $x$ -component of the electric field, b) The electron, proton (c) and oxygen (d) ion density distributions for  $t = 135$ ,  $a_0 = 20$ .

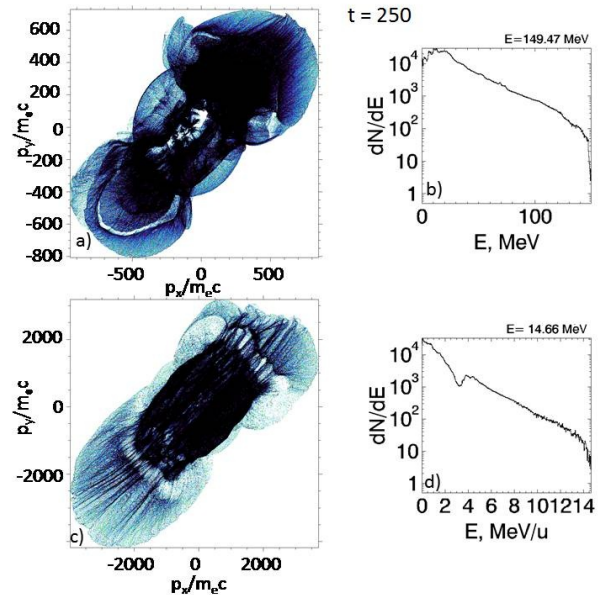


FIG. 15. The  $(p_x, p_y)$  phase distributions of protons (a) and oxygen ions (c), energy distributions of protons (b) and oxygen ions (d),  $a_0 = 20$ .

protons above 2 GeV and 6 GeV for oxygen ions for the target with  $n_{\max}/n_{\text{cr}} = 80$ . Using simple estimates for maximum ion energies gained in RPDA regime ([20], eq. (3)), we get lower values than observed in simulations, which could be caused by both Direct Coulomb Explosion and self-focusing of the laser pulse. The parts of the target that were not in touch with the main pulse exploded after the squeezing by the magnetic field. Fig. 16 shows how the magnetic field evolves in the case of



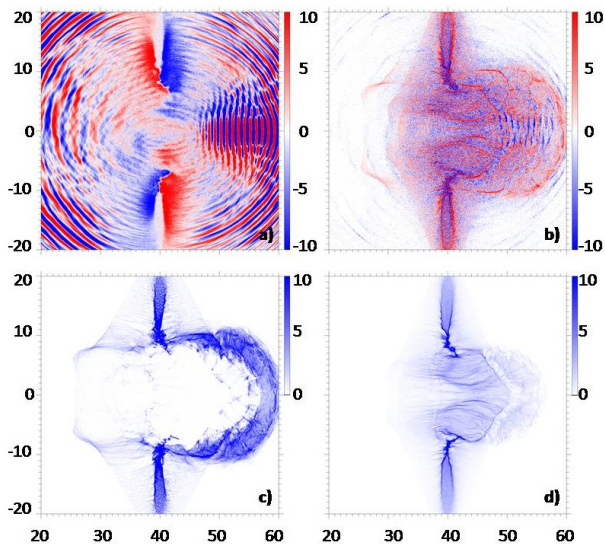


FIG. 16. The  $z$ -component of the magnetic field (a), the electric charge density (b), the proton (c) and the oxygen (d) density distributions in the  $(x, y)$  plane for the case of the laser pulse normal incidence on the target;  $a_0 = 134$ .

$a_0 = 134$  and  $n_{\max}/n_{\text{cr}} = 80$ . Being focused into the pre-plasma, the maximum field amplitude increases at least by the factor of 1.5. Phase space distributions for ions can be seen on Fig. 17. It is noticeable that magnetic squeezing effect still takes place for the ions at high laser pulse intensities in the regions of the target, which are not in the direct contact with the laser pulse (see Fig. 17, hemispheres at  $(p_x, p_y)$  and  $(y, p_x)$  plots). Even though it did not give the most energetic ions, it still allows to reach 500 MeV level.

Scaling of the maximum ion energy with the peak laser power in the log-log scale is presented in Fig. 19. The simulations of different targets (with various corona configurations) are presented as color dots, the line represents the expected maximum energy from the simple analytical estimation from the typical maximum energies obtained from Coulomb explosion, see Eqn. 1 from [25]. Even though the maximum energy scales with the laser power  $\mathcal{E}$  as  $\sim \mathcal{P}^{1/2}$ , we still obtain the ion energies that are high enough for the moderate laser systems. For instance, using these corona-equipped targets, we can reach the proton energies up to 200 MeV which is of high importance for the applications in hadron therapy [3]. The oxygen ion energy is about 15 MeV/u with the use of the finite contrast 200 TW laser systems. In the limit of Petawatt laser systems (1 – 10 PW), which would be accessible in the nearest future at ELI-Beamlines project [37], we observe the shift to the foil acceleration by the radiation pressure rather than magnetic field amplified Coulomb explosion.

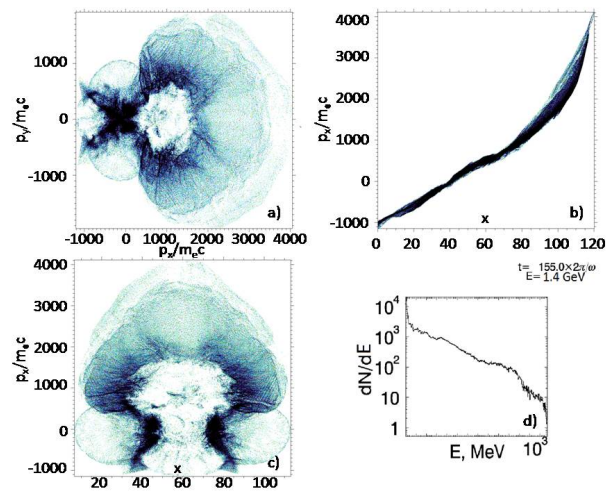


FIG. 17. The proton phase plots a)  $(p_x, p_y)$ , b)  $(x, p_x)$ , c)  $(y, p_x)$ , and d) the energy spectrum for  $t = 155$ ,  $a_0 = 134$  in the case of normal laser incidence on the target.

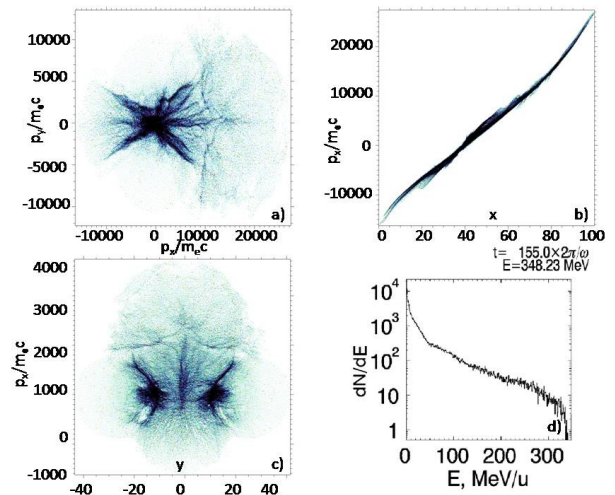


FIG. 18. The oxygen ion phase plots a)  $(p_x, p_y)$ , b)  $(x, p_x)$ , c)  $(y, p_x)$ , and d) the energy spectrum,  $a_0 = 134$  in the case of normal laser incidence on the target.

#### IV. CONCLUSION

Here by using the 2D PIC simulations we show that the configurations corresponding to the mass-limited targets surrounded by an underdense plasma corona exhibit a number of effects enhancing the maximum energy and increasing the total number of high energy ions. We observe the magnetic squeezing of the underdense parts of the target, when the pressure of self-generated quasi-static magnetic field pushes the electrons and ions into the target thus increasing the target plasma density. This effect has an important implication at the stage of the Coulomb explosion enlarging the achievable ion energy. While not giving the maximum energy in the whole fast

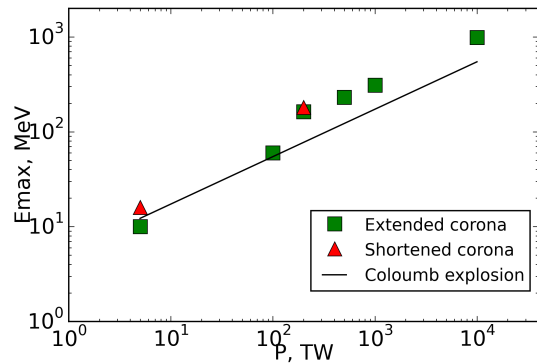


FIG. 19. Maximum proton energy at the peak of the laser pulse power: simulations with extended and shortened (exponential) corona vs theoretical curve for the Coulomb explosion ( $\mathcal{E}_p \approx 173\sqrt{\mathcal{P}}$ [petawatt] MeV, see [25]).

ion population, it is still a major factor in the proton acceleration as it allows to accelerate a substantial (large compared with the maximum energy isotropic component) number of protons up to energies that are an order of magnitude larger than the majority of protons are accelerated to.

Hole boring by the electric field arising due to the edge intensification and the plasma resonance at the sharp edge of the target is considered to be in strong correlation with the proton acceleration at the beginning of the interaction (before Coulomb explosions of the main target and preliminary compressed filaments come into play), providing the maximum proton energy at this interaction stage. Strong anisotropy of the proton acceleration in such a high-eccentricity ellipsoidal target is also an important feature that can be used for the generation of strongly collimated proton beams.

We also demonstrate that the presence of down-ramp density corona around the target can increase the maximum ion energies in comparison with flat density profiles.

## V. ACKNOWLEDGEMENTS

The authors thank M. Botton and A. Zigler for fruitful discussions. KVL expresses gratitude to M. Bussmann for the detailed comments on the early version of the work. This work was supported by the ELI Project No. CZ.02.1.01/0.0/0.0/15\_008/0000162. We also would like to acknowledge the support from Russian Foundation for Basic Research (grant No. 15-02-03063).

- 
- [1] M. Borghesi, J. Fuchs, S. V. Bulanov, A. J. Mackinnon, P. Patel, and M. Roth, *Fus. Sci. and Technology* **49**, 412 (2006); H. Daido, M. Nishiuchi, and A. S. Pirozhkov, *Rep. Prog. Phys.* **75**, 056401 (2012); A. Macchi, M. Passoni, and M. Borghesi, *Rev. Mod. Phys.* **85**, 751 (2013).
- [2] K. W. D. Ledingham and W. Galster, *New J. Phys.* **12**, 045005 (2010).
- [3] S. V. Bulanov, J. J. Wilkens, T. Zh. Esirkepov, G. Korn, G. Kraft, S. D. Kraft, M. Molls, and V. S. Khoroshkov, *Phys. Usp.* **57**, 1149 (2014).
- [4] S. V. Bulanov, T. Zh. Esirkepov, M. Kando, A. S. Pirozhkov, and N. N. Rosanov, *Phys. Usp.* **56**, 429 (2013).
- [5] S. V. Bulanov, T. Zh. Esirkepov, M. Kando, J. Koga, K. Kondo, and G. Korn, *Plasma Phys. Rep.* **41**, 1 (2015).
- [6] T. Kluge, W. Enghardt, S. D. Kraft, U. Schramm, K. Zeil, T. E. Cowan, and M. Bussmann, *Phys. Plasmas* **17**, 123103 (2010).
- [7] A. Zigler, S. Eisenman, M. Botton, E. Nahum, E. Schleifer, A. Baspaly, I. Pomerantz, F. Abicht, J. Branzel, G. Priebe, S. Steinke, A. Andreev, M. Schnuerer, W. Sandner, D. Gordon, P. Sprangle, and K. W. D. Ledingham, *Phys. Rev. Lett.* **110**, 215004 (2013).
- [8] E. Schleifer, Z. Henis, M. Botton, O. Shavit, D. F. Gordon, and A. Zigler, *Appl. Sci.*, **5**, 459 (2015).
- [9] K. Zeil, J. Metzkes, T. Kluge, M. Bussmann, T. E. Cowan, S. D. Kraft, R. Sauerbrey, B. Schmidt, M. Zier and U. Schramm, *Plasma Phys. Control. Fusion* **56**, 084004 (2014).
- [10] I. Last, I. Schek, and J. Jortner, *J. Chem. Phys.* **107**, 6685 (1997); T. Ditmire, J. Zweiback, V. P. Yanovsky, T. E. Cowan, G. Hays, and K. B. Wharton, *Nature (London)* **398**, 489 (1999); K. Nishihara, H. Amitani, M. Murakami, S. V. Bulanov, T. Zh. Esirkepov, *Nucl. Instrum. Meth. Phys. Res. A* **464**, 98 (2001); V. F. Kovalev and V. Yu. Bychenkov, *Phys. Rev. Lett.* **90**, 185004 (2003).
- [11] A. V. Gurevich, L. V. Parijskaya, and L. P. Pitaevskii, *Sov. Phys. JETP* **22**, 449 (1966).
- [12] S. Wilks, W. L. Kruer, M. Tabak, and A. B. Langdon, *Phys. Rev. Lett.* **69**, 1383 (1992).
- [13] P. Mora, *Phys. Rev. Lett.* **90**, 185002 (2003).
- [14] V. I. Veksler, *At. Energ.* **2**, 427 (1957).
- [15] T. Zh. Esirkepov, M. Borghesi, S. V. Bulanov, G. Mourou, and T. Tajima, *Phys. Rev. Lett.* **92**, 175003 (2004).
- [16] O. Klimo, J. Psikal, J. Limpouch, and V. T. Tikhonchuk, *Phys. Rev. ST Accel. Beams* **11**, 031301 (2008); A. P. L. Robinson, M. Zepf, S. Kar, R. G. Evans, C. Bellei, *New J. Phys.* **10**, 01302 (2008).
- [17] S. S. Bulanov, E. Esarey, C. B. Schroeder, S. V. Bulanov, T. Zh. Esirkepov, M. Kando, F. Pegoraro, and W. P. Leemans, *Phys. Rev. Lett.* **114**, 105003 (2015).
- [18] S. V. Bulanov, E. Yu. Echkina, T. Zh. Esirkepov, I. N. Inovenkov, M. Kando, F. Pegoraro, and G. Korn, *Phys. Rev. Lett.* **104**, 135003 (2010); S. V. Bulanov, E. Yu. Echkina, T. Zh. Esirkepov, I. N. Inovenkov, M. Kando, F. Pegoraro, and G. Korn, *Phys. Plasmas* **17**, 063102 (2010).
- [19] K. V. Lezhnin, F. F. Kamenets, V. S. Beskin, M. Kando, T. Zh. Esirkepov and S. V. Bulanov, *Phys. Plasmas* **22**, 033112 (2015).

- [20] S. S. Bulanov, A. Brantov, V. Yu. Bychenkov, V. Chvykov, G. Kalinchenko, T. Matsuoka, P. Rousseau, S. Reed, V. Yanovsky, D. W. Litzenberg, K. Krushelnick, and A. Maksimchuk, *Phys. Rev. E* **78**, 026412 (2008).
- [21] A. V. Kuznetsov, T. Zh. Esirkepov, F. F. Kamenets, S. V. Bulanov, *Plasm. Phys. Rep.* **27**, 211 (2001); S. V. Bulanov, D. V. Dyllov, T. Zh. Esirkepov, F. F. Kamenets, D. V. Sokolov, *Plasm. Phys. Rep.* **31**, 369 (2005); S. V. Bulanov, T. Zh. Esirkepov, *Phys. Rev. Lett.* **98**, 049503 (2007); A. Yogo, H. Daido, S. V. Bulanov, K. Nemoto, Y. Oishi, T. Nayuki, T. Fujii, K. Ogura, S. Orimo, A. Sagisaka, J.-L. Ma, T. Zh. Esirkepov, M. Mori, M. Nishiuchi, A. S. Pirozhkov, S. Nakamura, A. Noda, H. Nagatomo, T. Kimura, and T. Tajima, *Phys. Rev. E* **77**, 016401 (2008); S. S. Bulanov, V. Yu. Bychenkov, V. Chvykov, G. Kalinchenko, D. W. Litzenberg, T. Matsuoka, A. G. R. Thomas, L. Willingale, V. Yanovsky, K. Krushelnick, and A. Maksimchuk, *Phys. Plasmas* **17**, 043105 (2010); T. Nakamura, S. V. Bulanov, T. Zh. Esirkepov, and M. Kando, *Phys. Rev. Lett.* **105**, 135002 (2010); Y. J. Gu, Z. Zhu, X. F. Li, Q. Yu, S. Huang, F. Zhang, Q. Kong, and S. Kawata, *Phys. Plasmas* **21**, 063104 (2014).
- [22] Y. Fukuda, A. Ya. Faenov, M. Tampo, T. A. Pikuz, T. Nakamura, M. Kando, Y. Hayashi, A. Yogo, H. Sakaki, T. Kameshima, A. S. Pirozhkov, K. Ogura, M. Mori, T. Zh. Esirkepov, J. Koga, A. S. Boldarev, V. A. Gasilov, A.I. Magunov, T. Yamauchi, R. Kodama, P. R. Bolton, Y. Kato, T. Tajima, H. Daido, and S. V. Bulanov, *Phys. Rev. Lett.* **103**, 165002 (2009).
- [23] D. Haberberger, S. Tochitsky, F. Fiuza, C. Gong, R. A. Fonseca, L. O. Silva, W. B. Mori, C. Joshi, *Nature Phys.* **8**, 95 (2012); F. Fiuza, A. Stockem, E. Boella, R. A. Fonseca, L. O. Silva, D. Haberberger, S. Tochitsky, C. Gong, W. B. Mori, and C. Joshi, *Phys. Rev. Lett.* **109**, 215001 (2012); A. Macchi, A. S. Nindrayong, F. Pegoraro, *Phys. Rev. E* **85**, 046402 (2012).
- [24] G. A. Askar'yan, *Sov. Phys. JETP* **15**, 8 (1962); A. Litvak, *Sov. Phys. JETP* **30**, 344 (1970).
- [25] T. Zh. Esirkepov, J. K. Koga, A. Sunahara, T. Morita, M. Nishikino, K. Kageyama, H. Nagatomo, K. Nishihara, A. Sagisaka, H. Kotaki, T. Nakamura, Y. Fukuda, H. Okada, A. S. Pirozhkov, A. Yogo, M. Nishiuchi, H. Kiriyaama, K. Kondo, M. Kando, and S. V. Bulanov, *Nucl. Instrum. Meth. Phys. Res. A* **745**, 150 (2014).
- [26] T. Zh. Esirkepov, *Comput. Phys. Commun.* **135**, 144 (2001).
- [27] J. Braenzel, A. A. Andreev, K. Platonov, M. Klingsporn, L. Ehrentraut, W. Sandner, and M. Schnurer, *Phys. Rev. Lett.* **114**, 124801 (2015).
- [28] V. L. Ginzburg, *The Propagation of Electromagnetic Waves in Plasmas* (Pergamon, New York, 1964).
- [29] S. V. Bulanov, L. M. Kovrizhnykh, and A. S. Sakharov, *Phys. Rep.* **186**, 1 (1990).
- [30] G. A. Askar'yan and S. V. Bulanov, *Sov. Techn. Phys. Lett.*, **9**, 533 (1983).
- [31] L. D. Landau and E. M. Lifshitz, *Electrodynamics of Continuous Media* (Pergamon Press, Oxford, 1984).
- [32] S. V. Bulanov, M. Lontano, T. Zh. Esirkepov, F. Pegoraro, and A. M. Pukhov, *Phys. Rev. Lett.* **76**, 3562 (1996); T. Nakamura and K. Mima, *Phys. Rev. Lett.* **100**, 205006 (2008); L. Romagnani, A. Bigongiari, S. Kar, S. V. Bulanov, C. A. Cecchetti, M. Galimberti, T. Zh. Esirkepov, R. Jung, T. V. Liseykina, A. Macchi, J. Osterholz, F. Pegoraro, O. Willi, and M. Borghesi, *Phys. Rev. Lett.* **105**, 175002 (2010); F. Sylla, A. Flacco, S. Kahaly, M. Veltcheva, A. Lifschitz, V. Malka, E. d'Humieres, I. Andriyash, and V. Tikhonchuk, *Phys. Rev. Lett.* **110**, 085001 (2013).
- [33] S. V. Bulanov, N. M. Naumova, and F. Pegoraro, *Phys. Plasmas* **1**, 745 (1994).
- [34] V. Kumarappan, M. Krishnamurthy, and D. Mathur, *Phys. Rev. A* **67**, 043204 (2003).
- [35] V. A. Vshivkov, N. M. Naumova, F. Pegoraro, and S. V. Bulanov, *Phys. Plasmas* **5**, 2727 (1998).
- [36] T. Zh. Esirkepov, M. Yamagiwa and T. Tajima, *Phys. Rev. Lett.* **96**, 105001 (2006).
- [37] ELI-Extreme Light Infrastructure Science and Technology with Ultra-Intense Lasers Whitebook, Ed. by G. A. Mourou, G. Korn, W. Sandner, and J. L. Collier (THOSS Media, Berlin, 2011).